Investigation of volatile liquid surfaces by synchrotron x-ray spectroscopy of liquid microjets

Kevin R. Wilson
Department of Chemistry, University of California, Berkeley, California 94720

Bruce S. Rude
Advanced Light Source, Lawrence Berkeley National Laboratory, Berkeley, California 94720

Jared Smith, Chris Cappa, D. T. Co, and R. D. Schaller
Department of Chemistry, University of California, Berkeley, California 94720

M. Larsson
Department of Physics, SCFAB, SE-106 91 Stockholm, Sweden

T. Catalano
Advanced Light Source, Lawrence Berkeley National Laboratory, Berkeley, California 94720

R. J. Saykally[a)]
Department of Chemistry, University of California, Berkeley, California 94720

(Received 27 August 2003; accepted 1 December 2003)

Soft x-ray absorption spectroscopy is a powerful probe of surface electronic and geometric structure in metals, semiconductors, and thin films. Because these techniques generally require ultrahigh vacuum, corresponding studies of volatile liquid surfaces have hitherto been precluded. We describe the design and implementation of an x-ray experiment based on the use of liquid microjets, permitting the study of volatile liquid surfaces under quasi-equilibrium conditions by synchrotron-based spectroscopy. The liquid microjet temperatures are also characterized by Raman spectroscopy, which connects our structural studies with those conducted on liquid samples under equilibrium conditions. In recent experiments, we have observed and quantified the intermolecular surface relaxation of liquid water and methanol and have identified a large population of ''acceptor-only'' molecules at the liquid water interface. © *2004 American Institute of Physics.*
[DOI: 10.1063/1.1645656]

I. INTRODUCTION

Understanding the nature of chemical reactions that occur on liquid surfaces constitutes an active area of research that impacts many diverse fields, including geology, atmospheric chemistry, catalysis, and biology. A prerequisite for understanding surface chemistry is a detailed knowledge of the liquid surface itself. Yet, despite the enormous amount of thermodynamic data accumulated for liquid surfaces of pure solvents and binary solutions, a comprehensive microscopic description of liquid/vapor interfaces remains elusive. There are relatively few experimental techniques that can provide such molecular level detail, and as a result, much of what is known about interfacial structure is derived from computer simulations. For example, Braslau *et al.*[1] determined the thickness of the liquid water interface to be ~3.2 Å. Several groups[2–5] have exploited sum-frequency-generation (SFG) spectroscopy to identify unique surface vibrational resonances, as well as molecular orientation for a variety of liquid/vapor, liquid/liquid, and liquid/solid interfaces. Molecular-beam scattering studies reported Nathanson and co-workers[6] have explored the influence of microscopic surface corrugation on collision dynamics. Together, these techniques have provided important insights into the nature of liquid/vapor interface as well as valuable benchmarks for the development of improved computer simulations of molecular liquids. Recent molecular dynamics (MD) computer simulations have predicted some interesting interfacial phenomena that have yet to be observed experimentally. For example, the surface of simple salt solutions is predicted to be enriched in large polarizable anions, and are thought to engender ion-enhanced heterogeneous chemistry in the troposphere.[7,8] This prediction is contrary to conventional notions of interfacial adsorption, in which ions increase the surface tension of water and are thereby expected to exhibit negative adsorption.[9] It would be interesting to test these predictions against suitably detailed experiments.

X-ray absorption spectroscopy (XAS) comprises an array of powerful techniques for probing the electronic and geometric structure of metals, semiconductors, insulators, and adsorbates. In the soft x-ray region, where second-row elements absorb, these methods generally require UHV conditions. The use of liquid microjets, as introduced by Faubel *et al.* for ultraviolet photoelectron spectroscopy[10] not only allows the convenient introduction of volatile liquid samples into high vacuum, but also provides a clean, continuously replenished liquid surface, thus minimizing the severe prob-

a)Author to whom correspondence should be addressed; electronic mail: saykally@uclink4.berkeley.edu

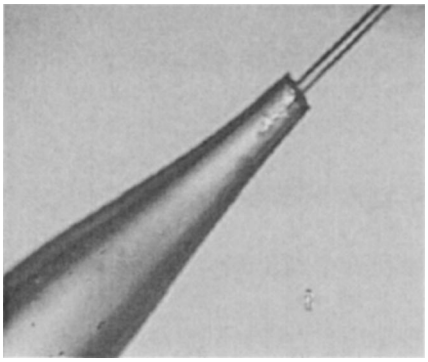

FIG. 1. A 10× microscope image of a 100 μm ID fused-silica capillary pulled by a micropipette puller to make a 20-μm-diam liquid jet nozzle.

lem of surface contamination. This article describes the development of XAS for the study of volatile liquid surfaces using microjets, and is organized as follows. Section II describes the fabrication and operation of glass microjet nozzles, which differ from those used in the original microjet studies reported by Faubel *et al.*[10] Section III details experiments characterizing the temperature of liquid water and methanol streams injected into high vacuum through microjet nozzles. Section IV outlines the design and implementation of the endstation used for XAS studies of liquid microjets. Finally, Section V presents a number of recent examples from our studies, illustrating the general utility of XAS to probe the molecular nature of liquid surfaces.

II. MICROJET NOZZLES

Our liquid microjet nozzles are fabricated from standard 100-μm-i.d. fused-silica capillaries purchased from a liquid chromatography vendor (Western Analytical Inc.). These capillaries are then pulled to the desired final nozzle diameter (500 nm to 50 μm) with a commercial CO_2 laser micropipette puller (Sutter 1000). The micropipette puller allows fine control over virtually every nozzle parameter, including final aperture size, taper length, and cone angle. In our initial studies, we used Pt/Ir electron microscope apertures available commercially (Ted Pella, Inc.), following Faubel *et al.*[10] However, it was found that laser-pulled fused silica nozzles are more reliable than Pt/Ir nozzles, which degrade over time due to electrochemical corrosion. We note that Faubel *et al.*[11] and later Holstein *et al.*[12] have investigated the charging characteristics of both metallic and fused-silica nozzles. The nozzles used in the present study have been characterized by optical microscopy to be 20 ± 1 μm in diameter, an example of which is shown in Fig. 1. A flow rate (F) of 0.5 ml/min imparts the liquid stream (20 μm diameter), pressurized to ~36 atm, with a velocity (ν_{jet}) of 38 m/s, determined geometrically from

$$\nu_{\mathrm{jet}} = F/(\pi r_0^2),$$

where r_0 is the microjet radius. The flow of liquid water through the 20-μm-diam nozzle can be characterized by a Reynolds number (R_e) given by

$$\frac{2\nu_{\mathrm{jet}} r_0 \rho}{\eta} = 953,$$

where ρ is the density (1000 kg/m^3), and η the viscosity of water (7.97×10^{-4} kg m^{-1} s^{-1}). $R_e<2000$ indicates that the flow under these conditions is laminar. In practice, the laminar region is observed to extend 5–10 mm in length, beyond which the jet (due to Rayleigh instabilities) breaks up into a tightly collimated stream of droplets extending >30 cm in length. Further studies of nozzle design (cone angle, taper length, etc.) which might influence the flow characteristics of these microjets are currently ongoing in our laboratory. In the experiments detailed here, the nozzle is inserted into an appropriate high-vacuum system and functions reliably for 60+ hours of stable operation. It should be noted that the length of the laminar flow region remains constant under vacuum, providing a well-behaved, intact liquid surface suitable for spectroscopic investigations.

III. MICROJET TEMPERATURE

In order to directly compare our XAS results obtained for microjet surfaces with other measurements conducted under equilibrium conditions (e.g., SFG), the temperatures of these microjets have been characterized. In vacuum, the liquid microjets are expected to cool rapidly by evaporation. The small size of these jets preclude the use of thermocouples, as the undercooled jet can heterogeneously nucleate upon contact with thermocouples or any other surface present in the vacuum chamber. Therefore, temperature measurements were conducted noninvasively by Raman spectroscopy.

The frequency, position, and line shape of the fundamental Raman –OH stretching bands have been shown to be very sensitive to the local hydrogen-bonding environment in liquids such as water, methanol, and ethanol, which is itself a sensitive function of temperature.[13–16] In the case of liquid water, many groups, including D'Arrigo *et al.*[13] and Walrafen *et al.*,[16] have investigated this behavior and determined that one can measure the temperature of liquid water simply and reliably by measuring Raman band profiles. Previous measurements, extending from the supercooled region (−20 °C) to near boiling, provide evidence for an isosbestic point in liquid water; suggesting a temperature-dependent equilibrium between two distinct distributions of hydrogen-bonded water molecules. Although this interpretation still remains controversial, analysis of integrated band areas[17,18] can be used as a sensitive thermometer for the bulk liquid. Similarly, Muller *et al.*[19] have shown that the –OH stretching band position in liquid methanol and ethanol redshifts upon cooling, exhibiting a linear frequency dependence of band center with temperature ranging from 0° to 70 °C.

To establish microjet temperatures under high-vacuum conditions, a set of calibration curves for both liquid water and methanol were obtained in our laboratory. To obtain these curves, the total Raman scattering intensity, collecting both vertical and horizontal polarizations, was measured as a function of temperature, using a thermostated nozzle assembly with a 20-μm-diam jet operating under atmospheric pressure, for which minimal evaporative cooling is expected. This expectation was indeed confirmed by comparison of the microjet spectra with those obtained in previous studies of

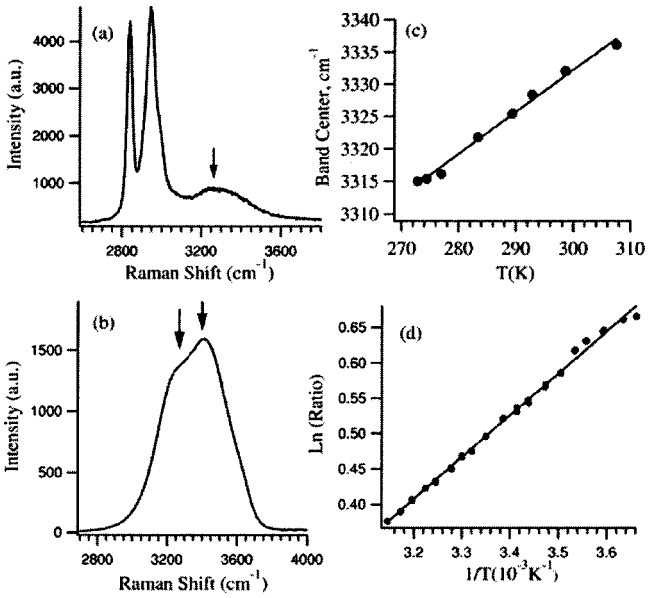

FIG. 2. Representative Raman spectra of liquid (a) methanol and (b) water. Calibration curves used in the determination of liquid temperature by Raman spectroscopy: (c) methanol and (d) water.

room-temperature liquid water and methanol.[13,19] The resulting calibration curves for liquid water and methanol are shown in Fig. 2. The calibration curve for water, using the method described by Davis *et al.*[18] and Vehring *et al.*,[17] was constructed by integrating the band area above and below 3400 cm^{-1}. The ratio of integrated band areas (below and above 3400 cm^{-1}) plotted versus $1/T$ yields a linear relationship. The fundamental OH band in liquid methanol lacks the structure found in liquid water and can be represented by a single Gaussian. The position of this band maximum was observed to redshift linearly with decreasing temperature [Fig. 2(a)], consistent with previous studies.[19]

Using the calibration curve in Fig. 2, we have undertaken a detailed study of bulk liquid temperature of the microjet as a function of residence time in vacuum. The vacuum chamber consists of a 2-3/4 in. cube (Kimball Physics) evacuated by a 110 1/s turbomolecular pump (Balzers TPU 110) located behind a liquid nitrogen trap. During normal operation of a 20 μm liquid water jet, the base pressure in the chamber is $\sim 10^{-4}$ Torr, which is conductance-limited due to the small dimensions of the vacuum chamber. The liquid jet is mounted on an *x,y,z* feed-through to optimize alignment during optical studies and is dumped into a liquid nitrogen trap located 50 cm from the nozzle. The cube is equipped with viewports, allowing optical access of the laser beam for Raman studies. A 200 mW, 514 nm cw laser beam is focused to ~ 40 μm^2 spot by a 3 mm focal length lens mounted inside the vacuum chamber. The total Raman scattering intensity, (collecting both vertical and horizontal polarization) is then recollimated at 90° from the incident beam, filtered, and refocused into a fiber-optic coupled 0.25 m monochromator, and detected by a liquid-nitrogen-cooled CCD camera (Roper Scientific).

Raman spectra were measured as function of distance from the nozzle at a specified jet velocity. The temperatures reported here consist of measurements obtained in the laminar as well as in the break-up regions of the liquid stream. After deconvolution, the bulk liquid temperature is plotted as a function of distance (or interaction time), as shown in Figs. 3 and 4 for liquid methanol and water, respectively. In general, the temperatures measured for liquid water and methanol depend nonlinearly on residence time, as expected, methanol exhibits much lower temperatures than water due to its higher volatility ($P_{water} = 17.5$ Torr versus $P_{meth} = 99.0$ Torr at 20 °C). Small-diameter jets exhibit much lower temperatures than do their larger counterparts; for example, as much as a 40 K temperature differential, in the break-up region, at an interaction time of 200 μs. Specifically, a 2.5-μm-diam water jet is observed to supercool to -37 ± 2 °C for an interaction time of ~ 300 μs, exhibiting no spectral evidence for ice nucleation. The corresponding cooling rate can be estimated to be $\sim 10^5$ K/s for a 4-μm-diam water jet, which is consistent in magnitude with results reported for microjet surfaces measured via molecular-beam sampling of the evaporates.

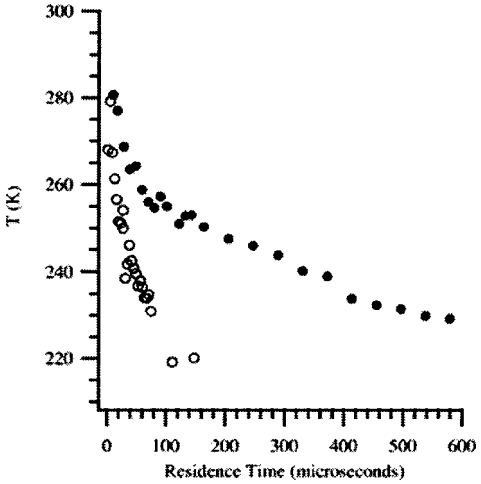

FIG. 3. Axial temperature profile of 21 (solid circles)- and 4 (open circles)-μm-diam methanol jets obtained by Raman spectroscopy.

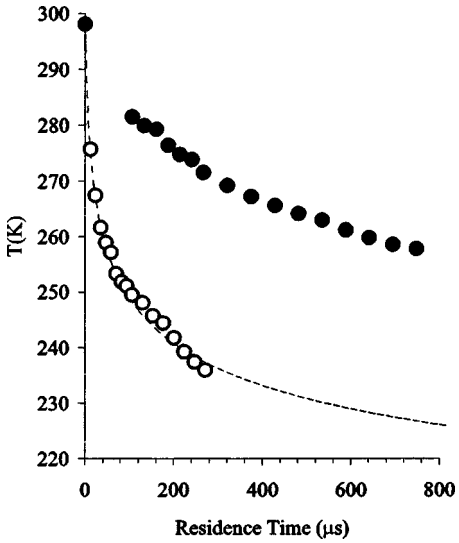

FIG. 4. Axial temperature profile of 21 (solid circles)- and 2.5 (open circles)-μm-diam water jets obtained by Raman spectroscopy. Solid line is obtained from numerical integration of Eq. (1) using $r_{ref} = 0.1098$ cm/s.

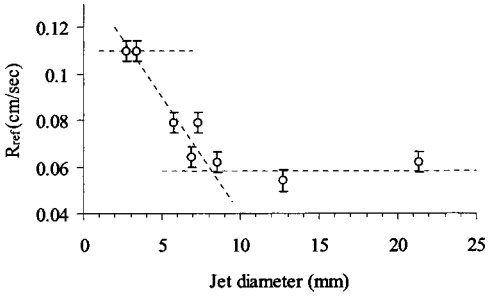

FIG. 5. Radial ablation rates [r_{ref}(cm/s)], at $T_{\mathrm{ref}}=277$ K obtained from a best fit of the experimental temperature profile of liquid water plotted against jet diameter. Solid lines are merely a guide to the eye and illustrate three distinct regions.

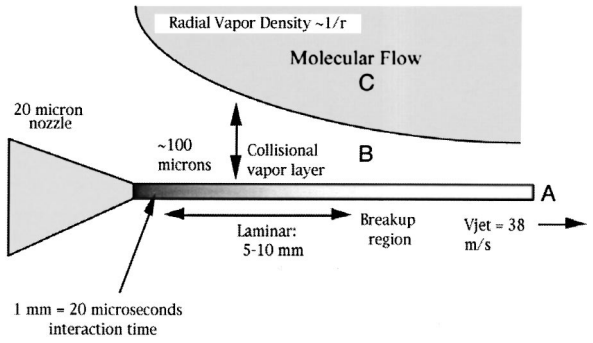

FIG. 6. Schematic of a 20 μm liquid jet. The dense liquid core (A) is surrounded by a collisional atmosphere (B), the size of which depends upon jet diameter, and beyond which the number density of evaporating molecules drops as $1/r$ in a collision-free zone (C), depicted in gray-scale. The density of B as well as the liquid temperature itself can be modeled via the CC Eq. (1).

Also shown in Fig. 4 is a temperature profile computed by a Clausius–Clapeyron (CC) evaporative cooling model. As reported by Faubel *et al.*[10] the temperature profile along the axis (z) of a liquid microjet can be determined by numerically integrating the expression

$$\frac{dT_0}{dz}=-2\frac{\dot{r}_0(T_0)}{\nu_{\mathrm{jet}}}\frac{\Lambda}{C_p}r_0^{-1}, \tag{1}$$

where the temperature T_0 is a function axial position [z (cm)], jet velocity [ν_{jet} (cm/s)], heat of vaporization [Λ(J/mol)], specific heat [C_p (J/mol K)], and radial evaporative ablation rate [$\dot{r}_0(T_0)$ (cm/s)]. $\dot{r}_0(T_0)$ is the rate at which the radius of the jet decreases due to evaporation, and is treated as the product of the mean velocity of evaporating molecules (assumed to be Maxwellian distribution) and the ratio of gas to liquid phase number densities:

$$\dot{r}(T_0)=\sqrt{\frac{kT}{2\pi m}}\frac{\rho_v(T_0)}{\rho_l}. \tag{2}$$

Here, C_p, Λ, and ρ_v are assumed to be independent of temperature. Since the radial ablation rate [$\dot{r}_0(T_0)$] is proportional to ρ_v, which decreases with temperature according to the CC equation, Eq. (2) can be reformulated in terms of a reference or initial ablation rate $r_{\mathrm{ref}}(T_{\mathrm{ref}})$ as

$$\dot{r}_0(T_0)=r_{\mathrm{ref}}\sqrt{\frac{T_0}{T_{\mathrm{ref}}}}\exp\left[-\frac{\Lambda}{kT_{\mathrm{ref}}}\left(\frac{T_{\mathrm{ref}}-T_0}{T_0}\right)\right]. \tag{3}$$

For liquid water at $T_{\mathrm{ref}}=277$ K, the maximum kinetic rate at which the radius of the jet decreases due to evaporation is $r_{\mathrm{ref}}=0.09$ cm/s according to Eq. (2). From a best fit of the 2.5-μm-diam jet temperature profile, shown in Fig. 4, r_{ref} was determined to be 0.1098 cm/s. This implies, in the absence of molecules recondensing on the liquid surface, an ablation rate within 20% of the maximum kinetic rate (0.09 cm/s) computed from Eq. (2). For larger diameter jets, the evaporation model captures the overall functional form of the temperature profile, but predicts much lower absolute temperatures (using $r_{\mathrm{ref}}=0.09$ cm/s) than are actually observed experimentally. For these larger jets ($r_0>2.5$ μm), agreement can be obtained by fitting the initial ablation rate (r_{ref}) to the experimental data, as is shown for water in Fig. 5. For jet diameters greater than 10 μm, r_{ref} is observed to be $\sim$0.055 cm/s. This ablation rate is a factor of 2 smaller than what is observed for the 2.5- and 3.4-μm-diam jets. For jets with diameters between 3.4 and 10 μm, r_{ref} is observed to be intermediate between the maximum kinetic rate of evaporation in small jets and the asymptotic value of 0.055 cm/s observed for larger diameter jets. These three regions are indicated with lines in Fig. 5. Similar trends are observed for liquid methanol jets. It should be noted that the temperature measurements reported here for all jet sizes span the laminar as well as beyond the break-up region of the liquid jet in which the liquid consists of a monodisperse stream of droplets. We observe no temperature inflections, which might indicate a transition from cylindrical to spherical geometry. These aspects as well as implications for evaporation will be discussed in further detail in a forthcoming publication.

These results, discussed in light of the simple jet schematic depicted in Fig. 6, illustrate the interplay between r_0 and mean free path (λ), given by

$$\gamma[\mathrm{cm}]=c\cdot P_v[\mathrm{Torr}]^{-1}, \tag{4}$$

where $c=5.3\times10^{-3}$ Torr cm for water. For water at 4 °C, under an equilibrium vapor pressure of 4.58 Torr, $\lambda=11$ μm.[10] For $r_0<\lambda$, nearly collisionless evaporation is realized, which approaches the evaporative ablation limit ($r_{\mathrm{ref}}=0.09$ cm/s) predicted by Eq. (2). Under these conditions, evaporating molecules move directly from the liquid core (A) to a region (C), which is governed by molecular flow, as shown in Fig. 6. For the case of $r_0>\lambda$, ballistic evaporation is impeded because of molecular collisions occurring in the gas-phase sheath surrounding the microjet. This implies that region B in Fig. 6 has become sizable and directly limits evaporation by requiring gas-phase diffusion to occur, as evidenced by the observed smaller evaporation rates and warmer temperatures. For example, the diameter of the gaseous envelope (region B in Fig. 6) surrounding a 20 μm jet is calculated to be $5r_0$ thick and is the source of molecular collisions. Consequently, molecules in this region will make about, six collisions with other gaseous molecules as they traverse this sheath, beyond which the vapor density (region C in Fig. 6) decreases as the reciprocal of the distance from the jet.[10] Furthermore, Fuchs and Legge[20] showed that the temperature of millimeter-sized liquid jets is not determined by the base chamber pressure (10^{-3}–10^{-5} Torr)

measured at macroscopic distances from the jet, as expected from the CC equation, but rather the local environment immediately surrounding the jet. They observed the radial vapor flow from a 2-mm-diam jet to be supersonic, and point out that the physical properties of the jet itself cannot be influenced by the pressures measured at macroscopic distances.

For the XAS studies described subsequently, experiments were conducted on 15–20-μm-diam jets at an interaction time of 20 μs. At this position, the bulk liquid temperature is measured to be ~290 K for water and ~280 K for methanol. In general, evaporation is a rare event, occurring on a long time scale, compared to typical molecular motions. The maximum kinetic evaporation rate for water at 20 °C is 8.5×10^{21} molecules $\sec^{-1}\,\mathrm{cm}^{-2}$, or 8.5×10^{6} monolayers (ML) s^{-1}.[21] This corresponds to the evaporation of ~170 H_2O ML during an observation time of 20 μm, which constitutes a minute fraction of the molecules in a 20-μm-diam water jet.

It is perhaps surprising that a CC model correctly predicts the experimental 2.5 μm microjet temperature profile without explicitly accounting for thermal conduction into the liquid stream. This might imply counterintuitively that there is not an appreciable radial temperature gradient in these small jets, due to efficient mixing between the surface and bulk liquid. Recent evidence from steady-state evaporation experiments reported by Fang and Ward[22] indicate that during evaporation or condensation, a macroscopic surface layer of water exhibiting a nearly constant temperature profile is formed. The thickness of this interfacial isothermal layer is measured to be 200–600 μm,[23] beyond which the temperature is observed to increase linearly while moving into the bulk liquid, indicating heat transfer by thermal conduction. It should be pointed out that this isothermal surface layer is also predicted by statistical rate theory.[24] Ward and Stanga[23] postulate that efficient surface mixing, leading to this macroscopic isothermal layer, originates from either ''energy partitioning'' during evaporation or Marangoni–Benard convection-driven thermal conduction. Since the 2.5-μm-diam liquid jet is much smaller than the observed depth of this isothermal interfacial layer, it is perhaps not surprising that a simple CC evaporation model is adequate to account for our experimental observations.

The only other experimental temperature studies of microjets were those published by Faubel *et al.*[10] By careful positioning of a skimmer, Faubel *et al.*[10] were able to estimate the surface temperature of a variety of micron-sized jets by measuring the velocity distribution of molecules evaporating from the surface and fitting them to a floating Maxwellian. Their analysis is valid only when collisions among evaporating molecules can be suppressed, and the local temperature measured in the molecular beam can be directly related to the liquid surface temperature. Near-collisionless evaporation is observed when the jet size is reduced to dimensions smaller than the mean free path of water molecules ($r_0<\lambda$), as evidenced by the speed ratio (S) of the sampled molecular beam. Although such collisionless expansion is expected from point sources smaller than λ, some collisions will always persist in liquid microjets, since the length of the jet is larger than λ, as pointed out by Sibold and Urbassek.[25] A 5-μm-diam jet was reported to have surface temperatures as low as 210 K and cooling rates of $\sim1.7\times10^5$ K/s. For larger jets, however, Faubel *et al.*[10] report $S\gg1$, indicating that evaporating molecules undergo many collisions and supersonically expand from the liquid surface. In order to obtain reliable surface temperatures for these larger jets, a second skimmer was introduced perpendicular to the long axis of the jet minimizing collisions in the expanding vapor; effectively ''freezing'' out the translational degrees of freedom. For diameters of 20 μm and larger, only moderate evaporative cooling was reported, yielding surface temperatures between 298 and 273 K.

Sibold and Urbassek[25] studied the evaporation of particles into vacuum from cylindrical jets using hard-sphere Monte Carlo simulations of the Boltzmann equation. They directly simulated the 5 μm jet experiments conducted by Faubel *et al.*[10] and obtained a speed ratio ($S=1.71$) in good agreement with the experimental value ($S=1.69$). Given this result, and using the radial gas temperature reported by Faubel *et al.*,[10] they predict a liquid surface temperature of 300 K. Considerably lower surface temperatures were reported by Faubel ($T=210$ K), leading Sibold and Urbassek to conclude that the experimental value is more representative of the local gas temperature above the liquid surface, rather than the actual liquid surface temperature itself. This apparent discrepancy in surface temperature obtained by experiment and simulation still remains unresolved.

Recent theoretical and experimental studies of evaporation have called into question the classical molecular picture of evaporation and condensation. First, Fang and Ward[22] measured a sharp temperature discontinuity, using a 25 μm thermocouple, at the liquid/vapor interface during evaporation and condensation. The temperature of the vapor was observed to be higher than that of the liquid surface during all steady-state evaporation and condensation experiments, which is inconsistent with the predictions of classical kinetic theory and the computational results of Sibold and Urbassek,[25] in which the opposite temperature discontinuity is predicted. Second, Phillips *et al.*[26] argue that molecules evaporating from the liquid surface obey a non-Maxwellian velocity distribution. As a result, Ward and Stanga,[23] as well as Phillips[26] conclude that only molecules from the high-energy tail of the Boltzmann distribution actually escape from the liquid surface. In light of these recent developments, it is unclear whether the evaporation experiments reported by Faubel *et al.*[10] can be correctly described in classical terms.

The liquid temperature, as well as the vapor densities in regions B and C decrease with interaction time (distance from the nozzle) due to evaporative cooling, which we have shown can be modeled via the CC equation. One can imagine two extremes: (1) region B is negligible, and evaporation proceeds by ballistic molecular flow, unimpeded by collisions in the vapor immediately above the liquid surface, or (2) the collisional atmosphere is a continuum ($r_0\gg\lambda$) and evaporation is therefore limited by molecular diffusion through region B. This is the usual case for a (evaporating) liquid under atmospheric conditions. In general, liquid mi-

crojets ($r_0 > \lambda$) are systems in which region B cannot be entirely neglected or simply treated as a continuum. Unfortunately, flow under these conditions is not well described by available analytical techniques.[24]

For a 2.5-μm-diam jet, we observe a temperature profile consistent with the maximum kinetic evaporation rate, suggesting minimal contribution from region B. This observation is supported by Faubel *et al.*,[10] in which the speed ratio of the molecular beam emanating from these small jets is consistent with near-collisionless evaporation. Conversely, for $r_0 > \lambda$, Faubel *et al.*[10] observed supersonic expansion of evaporates, which clearly indicates the existence of a collisional atmosphere above the liquid surface. This is consistent with our temperature studies of larger jets (>10 μm diam) in which the evaporation rate is a factor of 2 smaller than the kinetic limit ($r_{\mathrm{ref}} = 0.09$ cm/s). In other words, as r_0 increases relative to λ, the evaporation rate becomes limited by diffusion through region B, approaching an asymptotic value of steady-state evaporation similar to that under atmospheric conditions.

IV. X-RAY ABSORPTION

X-ray absorption spectroscopy (XAS) is an ''atom-specific probe'' ideally suited for studies of the local electronic structure of disordered media. In the soft x-ray region, the $1s$ electron of N, C, or O atoms can be excited into unoccupied molecular orbitals, Rydberg states, or the continuum. Spectrally narrow features, which generally appear below the ionization potential (IP), result from excitations into antibonding molecular orbitals or Rydberg states, and are termed near-edge x-ray absorption fine structure (NEXAFS). These features are extremely sensitive to molecular orbital changes resulting from the formation of a chemical or hydrogen bond (HB), a change in oxidation state, or in thermodynamic phase. Recently, the NEXAFS spectra of liquid water and ice have been used to examine the rehybridization of these antibonding molecular orbitals resulting from HB formation.[27]

The region lying more than ~50 eV above the IP, wherein the final state consists of a free photoelectron and core hole, exhibits extended x-ray absorption fine structure (EXAFS). An EXAFS spectrum [$\chi(k)$] consists of broad oscillations in the absorption coefficient that arise from final-state interference effects due to backscattering of the photoelectron from neighboring atoms. Within the single-scattering formalism, modulation in the absorption coefficient ($\Delta\mu$) for *K*-edge spectra normalized to the isolated atomic background (μ_0) is

$$\chi(K) = \frac{\Delta\mu}{\mu_0} = -\sum_j \frac{S(k)N_j}{kr_j^2} |f_i(k,\pi)| \times \sin[2kr_j + \varphi_j(k)] e^{-2\sigma_j^2 k^2}, \quad (5)$$

where N_j is the number of nearest neighbors, k the photoelectron wavevector, f_j the scattering amplitude, $S(k)$ is the amplitude reduction term due to many-body effects, and r_j is the radial distance from the absorbing atom. Mean-square fluctuations in r_j are accounted for in the exponential Debye–Waller factor by σ_j, and $\varphi_j(k)$ accounts for the total phase of the curved wave scattering amplitude along the scattering trajectory. Contributions from all other scattering paths can be represented in a similar way. EXAFS spectra, which are generally easier to interpret than NEXAFS, yield local structural information such as near-neighbor distances, as well as coordination numbers. There is an increasing theoretical and experimental effort dedicated to EXAFS analysis of liquids, amorphous solids and glasses.[28,29]

A. Detection of x-ray "action" spectra of liquid microjets

The XAS absorption coefficient can be probed directly, as in traditional transmission experiments, or indirectly, by detecting the emission of secondary electrons, ions, neutrals, or fluorescent photons produced by the accompanying Auger decay.[30] Furthermore, each of these emitted particles have characteristic escape depths.[31] For example, fluorescent photons have an escape depth of many microns, while secondary electrons, which dominate the total electron yield (TEY), escape from an average depth of 20 Å, determined by the average kinetic energy distribution (<20 eV). Ions, atoms, or molecules desorb directly from the interface—sensitive to only the outermost surface layer (1–5 Å).[32] By separately measuring the total ion yield (TIY) and TEY as a function of x-ray excitation energy, XAS spectra of the liquid surface and bulk can be obtained simultaneously. We have observed little difference between the NEXAFS spectrum measured by TEY and fluorescence yields for liquid water, indicating that bulk electronic properties are probed in both cases. As liquid samples become more complex (e.g., binary mixtures, aqueous solution, bimolecular gels), time-of-flight mass spectrometry, ion–electron coincidence, and photoelectron detection schemes can be easily incorporated into our experiment, yielding further insights into environmentally and technologically relevant samples.

B. Description of synchrotron endstation

Conducting experiments on volatile liquid surfaces at synchrotron facilities imposes some unique constraints upon the experimental design, in particular the vacuum system. Working in the soft x-ray region (100–1500 eV) requires a UHV environment with a beamline base pressure of 5×10^{-10} Torr, as well as a hydrocarbon-free environment. High-throughput, oil-based diffusion pumps, routinely used by other groups[33,34] in multiphoton studies of liquid microjets cannot be utilized, as they present an unacceptable risk of hydrocarbon contamination of the x-ray optics contained within the beamline and the storage ring. Consequently, an endstation was specially designed to allow windowless coupling of the x-ray beam onto liquid microjets of volatile solvents, such as water or alcohol. These experiments were conducted on Beamline 8.0 at the Advanced Light Source, Lawrence Berkeley National Laboratory. The endstation consists of three sections, delineated by base pressure, and is depicted schematically in Fig. 7. Section A consists of three differentially pumped stages (A1, A2, A3), while B houses the liquid microjet as well as charged-particle detectors.

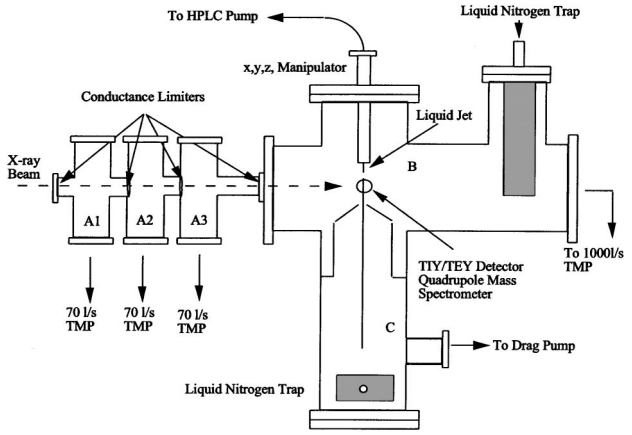

FIG. 7. Liquid microjet endstation schematic (not to scale).

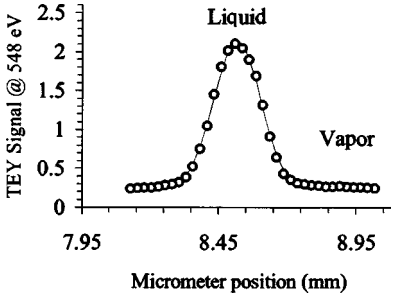

FIG. 8. TEY profile of a 20-μm-diam jet obtained by translating the liquid stream through the focused x-ray beam at 548 eV. The Gaussian FWHM is determined to be 202 μm, which is limited by the x-ray spot size. A 10× enhancement of the liquid signal over the vapor background is clearly observed, consistent with the estimated absorption strengths of vapor vs liquid.

The first section (A) is interfaced directly to the beamline and is designed to eliminate all vacuum load originating at the microjet that might otherwise contaminate the x-ray optics of the beamline. This section consists of three vacuum chambers, each separated by a 2-mm-diam conductance limiter and individually pumped by a 70 1/s (Varian V70) turbopump; these are all backed by a single 100 1/s drag pump, which in turn is backed by a 4 1/s diaphragm pump (Drytel 100). This section is mounted first to the beamline and baked for 12–20 h to achieve a base pressure in each section of $\sim 5\times10^{-10}$ Torr. This entire assembly is mounted on a stand with six degrees of freedom to facilitate the alignment of the entire vacuum vessel around the focused x-ray beam. For convenience, the x-ray beam is usually aligned first through this section, after which vacuum connections are made to sections B and C.

Section B, which is separated from A by a 5 mm conductance limiter, houses the interaction chamber in which the x-ray beam intersects the microjet at 90°. This section is pumped by a 1000 1/s turbopump (Leybold 1000C) backed by a 50 cubic feet per minute (CFM) rotary vane pump (Alcatel 2063). The turbo pump is protected from condensables by a liquid nitrogen trap, allowing the pump to be operated at the maximum rotational speed. The degassed liquid jet is introduced into the chamber by a standard HPLC pump (Knauer K-1001) through a *x,z,y* vacuum feed-through. Fine control of the liquid jet orientation is necessary, as achieving proper overlap of the 80×200 μm x-ray spot with the 20 μm jet is nontrivial. The microjet then travels ~4 mm before entering a 300- or 500-μm-diam skimmer, separating section B from C, finally condensing on a liquid nitrogen trap 1 m away. The skimmer is mounted on bellows, allowing the entire assembly (microjet and aperture) to be moved together while aligning the x-ray beam to the microjet. This aperture also serves to minimize the gas load, as well as backscattered liquid particles emanating from section C, which is typically operated at higher pressures than B. For total yield measurements, copper electrodes are mounted 2 mm from the jet axis, and are biased appropriately for either ions or electrons. A photodiode is also mounted in the line of sight of the microjet and is used to measure the total fluorescence yield.

The interaction region is also equipped with a quadrupole mass spectrometer (UTI 100C) that has been modified to detect ions produced by core-level excitation of the liquid jet. The entrance aperture to the spectrometer is positioned at 3 mm from the liquid jet and consists of a three-element Einzel lens that both extracts and focuses the ions coaxially into the filtering rods. The ions are detected either with a channeltron electron multiplier or Faraday cup. To enhance the signal-to-noise ratio, lock-in detection was employed by modulating the incoming x-ray beam with a tuning fork chopper operating at 1 kHz (Electro Optical Products, Inc.)

Finally, the microjet terminates on a liquid nitrogen trap located in section C. A second liquid nitrogen trap is positioned below the first to catch ice particulate or supercooled alcohol that accumulates during the course of the experiment. This section is pumped by a 20 1/s drag pump (Drytel 20) during start up, but can be valved out during normal operation. Sections B and C are mounted on a stand that facilitates course alignment of the endstation around the x-ray beam.

During normal operation, a 20-μm-diam liquid water microjet is pressurized to ~500 psi (36 atm). The typical pressures in each of sections A, B, and C are as follows: C is maintained at <1 mTorr, while B (the interaction region) is stable at 2×10^{-5} Torr. Moving upstream to the beamline, the first section of differential pumping (A3), is 2×10^{-6} Torr, dropping to 3×10^{-8} Torr in section A2 with an operating pressure of 8×10^{-10} Torr in the final section labeled A1. For 20-μm-diam alcohol (e.g., methanol) microjets the pressures are typically a factor of 4 higher, consistent with the difference in equilibrium vapor pressures.

Shown in Fig. 8 is a profile of the liquid jet obtained by translating a 20-μm-diam jet through the x-ray beam and measuring the TIY or TEY signals excited by 548 eV photons. The Gaussian full width at half-maximum (FWHM) of the profile is 202 μm (limited by the x-ray spot size) with a 10× enhancement of the condensed phase signal over the background vapor. This illustrates that the liquid can be probed without significant interference from the vapor, which both attenuates the incoming x-ray beam and scatters the outgoing charged particles. Faubel *et al.*[35] showed that a high-quality ultraviolet photoelectron spectra of liquid water could be obtained in a similar experimental configuration. In addition, Kondow *et al.*[34] showed vapor-phase interference to be negligible when using high-velocity liquid microjets

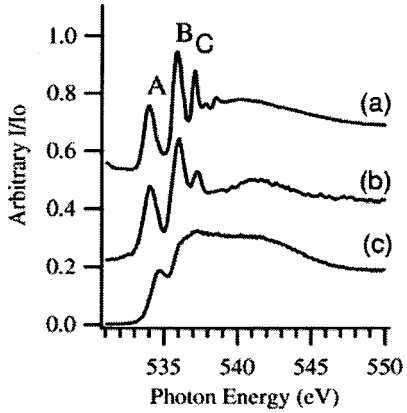

FIG. 9. TIY NEXAFS spectra of (a) water vapor measured 4 cm away from the liquid jet. NEXAFS spectra of a 20-μm-diam liquid water microjet measured by (b) TIY and (c) TEY (from Ref. 38).

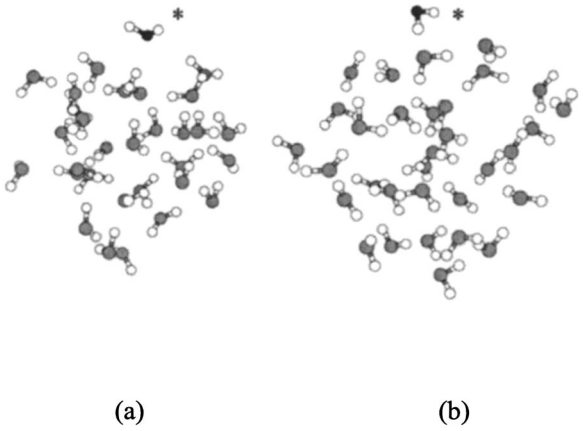

FIG. 10. Snapshots of two molecular clusters generated by classical MD simulations depicting two representative surface species (denoted with an asterisk): (a) acceptor-only and (b) single-donor hydrogen-bonded molecules (from Ref. 38).

for resonance enhanced multiphoton ionization studies of liquid surfaces.

The equivalent vapor thickness (β) or column density surrounding the liquid jet (treated as a slit source) can be described as[10]

$$\beta = \int_{r_0}^{r} \left(n_0 \frac{r_0}{r} \right) dr = n_0 r_0 \ln\left(\frac{r}{r_0} \right), \tag{6}$$

where n_0 is the vapor density above the liquid surface, r_0 the radius of the jet, and r the radial distance from the source. The attenuation of the incoming x-ray beam due to this vapor blanket is given by

$$\frac{I}{I_0} = e^{-\sigma\beta}, \tag{7}$$

where σ is the oxygen (O) K-edge absorption cross section. Given the O K-edge cross section (0.5 Mb at 532 eV) and assuming n_0 to be 20 Torr (the equilibrium vapor pressure of water at 298 K), the transmission (I/I_0) of the x-ray beam through a 10 cm path length (the dimension of the vacuum chamber) is ~87%. Therefore, we can estimate that at most 13% of our measured electron or ion signal is due to the vapor immediately surrounding the jet, consistent with the microjet profile shown in Fig. 8.

V. XAS OF LIQUID MICROJETS

A. Surface NEXAFS of liquid water

Surface hydrogen bond (HB) configurations of liquid water, which determine many important interfacial properties (for example, surface tension and interfacial mobility), remain incompletely characterized. Shen and co-workers[36] interpret a SFG vibrational band contour as being consistent with a free O–H oscillator or dangling bond at the liquid water surface. They estimate, by titrating the surface with an alcohol, that >20% of the surface population is due to single hydrogen-bonded donor molecules with one free–OH extending from the interface by ~38°. MD simulations have found orientational populations consistent with these SFG results.[37] Reproduced in Fig. 9 are TIY and TEY NEXAFS spectra of a 20-μm-diam liquid water jet.[38] For comparison, a spectrum of water vapor is also shown, measured with the microjet moved 4 cm away from the x-ray beam. The broad TEY NEXAFS spectrum from the microjet is consistent with bulk sensitive x-ray Raman scattering,[39] fluorescent yield,[27] and Auger electron studies[40] of liquid water measured under equilibrium conditions. However, the surface-sensitive TIY spectrum retains much (but not all) of the fine structure observed in the gas phase.[41] The sharp peaks in the gas-phase spectrum, labeled A and B, arise from transitions of the $1s$ electron located primarily on the oxygen atom to the $4a_1$ and $2b_2$ antibonding molecular orbitals, respectively. Peak C has been assigned to a Rydberg state of symmetry $^1B_1$. Under dipole selection rules, the O p character of these sp-hybridized molecular orbitals are directly probed in XAS. Since the $4a_1$ and $2b_2$ states are antibonding molecular orbitals polarized toward the hydrogen atoms, these states are expected to be extremely sensitive spectroscopic probes of the varieties of HBs present at the liquid surface. Myneni *et al.*[27] have shown that the XAS spectrum of bulk water shows the largest perturbation when a HB is broken on the donor side of the molecule, breaking the tetrahedral HB symmetry found in liquid water or ice.

To explore the ability of the TIY NEXAFS spectrum of liquid water to probe the HB structure at the surface, the Stockholm group[42] generated two surface HB configurations using MD simulations and density functional theory (DFT) spectral calculations, as reported in Ref. 38. Shown in Fig. 10 are two surface clusters obtained from snapshots of classical MD simulations, highlighting an acceptor-only and single-donor surface molecule (depicted with an asterisk). The respective oscillator strengths for these surface species were computed with DFT and are shown in Fig. 11. Also included in Fig. 11 is the H+ NEXAFS spectrum of amorphous ice measured by Coulman *et al.*[43] One can clearly see the incipient formation of a broad ''conduction band'' in the computed single-donor molecule spectrum, as the relative intensities of the $4a_1$ and $2b_2$ orbitals are greatly reduced. The spectrum computed for the single-donor species captures the main features of the amorphous ice surface and is consistent with previous infrared studies of large amorphous ice

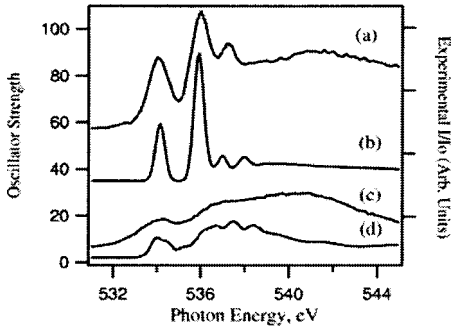

FIG. 11. NEXAFS spectra of the: (a) liquid water surface measured by TIY and (c) amorphous ice surface measured by H+ yield (see Ref. 43). NEXAFS spectra of (b) acceptor-only and (d) single-donor surface molecules computed from the configurations shown in Fig. 9.

particles.[44] Conversely, the spectrum computed for the acceptor-only surface molecule exhibits very little change from that of an isolated molecule and illustrates the extreme sensitivity of XAS to the presence of donor HBs. The close correspondence of the computed acceptor-only spectrum with that of the experimental TIY spectrum, shown in Fig. 11, leads to conclusion that there is indeed a large fraction of molecules residing at the liquid water surface having two broken donor HBs. The liquid surface thus consists of an ensemble of molecular configurations including fully coordinated molecules as well as the single-donor species as detected by SFG. The TIY NEXAFS spectrum can be decomposed into a superposition of such configurations, but the presence of sharp fine structure remains a conclusive fingerprint of the acceptor-only species.

B. Surface EXAFS of liquid water and methanol

Radial distribution functions (RDFs) obtained by neutron and x-ray diffraction are important tools for the elucidation of ''liquid structure.'' The close correspondence of RDFs obtained in scattering experiments to the $G(r)$ values computed in MD simulations have led to refined liquid force fields and an enhanced understanding of the microscopic nature of bulk liquids. The development of nonlinear optical techniques has enabled vibrational spectroscopy of liquid surfaces, making it possible to obtain relatively detailed vibrational and orientational information for liquid surfaces.[45,46] Scattering studies of liquid interfaces are complicated by the large equilibrium vapor above most liquids, as well as by the necessity for monolayer sensitivity. Nathanson and co-workers[47,48] have elegantly circumvented this problem by working with low-vapor-pressure liquids (e.g., supercooled sulfuric acid, glycerol, etc.) that are compatible with the high-vacuum conditions necessary for molecular-beam studies.

EXAFS spectroscopy has been used to investigate local structure in many studies of atomic liquids, glasses, and aqueous solutions.[49] It is a short-range probe, limited to <10 Å from the absorbing atom mainly due to inelastic scattering losses of the outgoing photoelectron.[50] By applying the surface sensitivity of TIY EXAFS to liquid microjets, near-neighbor distances, and coordination numbers can now be obtained for surfaces of hydrogen-bonding liquids. In a recent publication,[51] our group reported the surface relaxation of the O–O distance in both liquid water and methanol. Shown in Fig. 12 are the extracted EXAFS oscillations $[\chi(k)]$ for liquid water measured by TEY and TIY. The oscillations were analyzed within the single-shell approximation by standard analysis software.[52] The model fits to the raw EXAFS oscillations are also shown in Fig. 12. The O–O distance in bulk water measured by TEY is found to be 2.80 ± 0.05 Å, in good agreement with previous x-ray diffraction[53,54] and x-ray Raman EXAFS[39] results. The interfacial O–O distance determined by TIY is 2.96 ± 0.05 Å. This result indicates that there is a 5.9% expansion in the O–O distance at the interface of water.

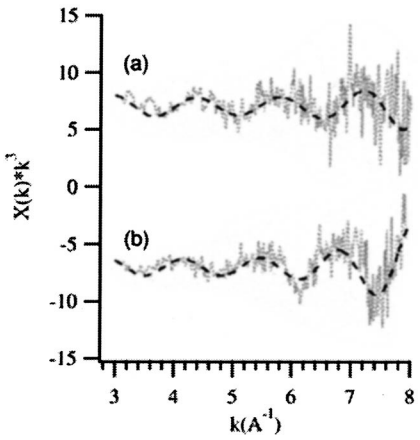

FIG. 12. EXAFS spectra $[k^3\chi(k)$ vs $k]$ of liquid water obtained by (a) TEY and (b) TIY detection techniques. Dashed lines are model fits to the experimental EXAFS oscillations using the single scattering EXAFS Eq. (5) as reported by Wilson *et al.* (see Ref. 51).

The expansion of the average O–O distance at the liquid water surface, along with our identification of a group of HB acceptor-only surface species, implies a significant relaxation of the electronic perturbation due to intermolecular HBs at the liquid/vapor interface.[38] This can be rationalized by an overall reduction in the number of surface HBs per water molecule, as predicted by MD simulations,[37,55–57] as well as lengthening of the near-neighbor distance, which would weaken the remaining HBs between surface molecules. This view implies an interfacial layer in which water molecules exhibit enhanced mobility, as evidenced by an interfacial diffusion constant computed to be $\sim 54\%$ larger than the bulk value.[56]

Conducting the same analysis outlined earlier and described in detail by Wilson *et al.*,[51] intermolecular EXAFS oscillations for the liquid methanol surface and bulk are shown in Fig. 13. The interfacial O–O distance, determined by analysis of the TIY EXAFS oscillations, is 2.62 ± 0.05 Å. The bulk value, by analysis of TEY EXAFS is 2.75 ± 0.05 Å, in good agreement with previous diffraction studies.[58,59] Hence, the R_{O-O} distance at the liquid methanol surface is observed to contract by 4.6%, exhibiting a behavior opposite to that of liquid water.

In contrast to water, the surface vibrational spectrum of liquid methanol shows no evidence of a ''free OH'' bond.'' [60] The ''bonded OH stretching'' region exhibits a vibrational band that is much narrower than and redshifted from the bulk

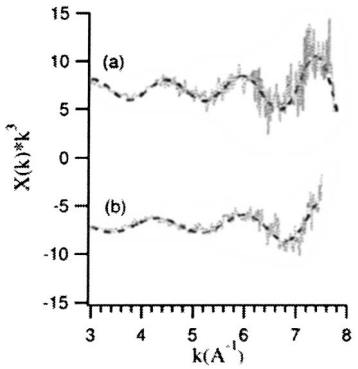

FIG. 13. EXAFS spectra $[k^3\chi(k)$ vs $k]$ of liquid methanol obtained by (a) TEY and (b) TIY detection techniques. Dashed lines are model fits to the experimental EXAFS oscillations using the single scattering EXAFS Eq. (5) as reported by Wilson *et al.* (see Ref. 51).

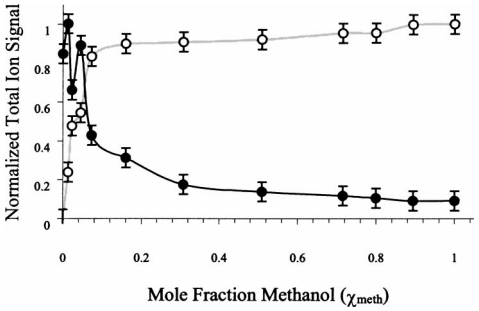

FIG. 14. Methanol/water surface adsorption isotherms (at 548 eV) measured by mass-resolved ion yield. TIY of methanol (open circles) and water (solid circles) as a function of bulk methanol mole fraction χ_{meth}. Methanol and water ion signals have been normalized to the pure liquids. Lines are a guide to the eye.

liquid infrared spectrum. The close correspondence of the SFG spectrum to that measured for solid methanol led Stanners *et al.*[60] to conclude that the surface of liquid methanol is ''ice-like.'' The O–O distance in solid methanol has been previously determined[61,62] by diffraction methods to be 2.66 Å, implying a shorter HB length than in the liquid, which is consistent with the observed redshifted vibrational spectrum. The surface R_{O-O} for liquid methanol measured by TIY EXAFS (2.62 ± 0.05 Å), is in close agreement with that of methanol ice. Solid methanol contains molecules arranged in parallel hydrogen-bonded chains with an average of two HBs per molecule. The close correspondence of the O–O distance and vibrational spectrum of the liquid surface with that of solid methanol leads to the conclusion that a similar HB topology is present at the liquid surface. The strong orientation of the methyl group in the outermost surface layer naturally implies an oppositely oriented adjacent layer below the surface. This ''hydrophobic packing'' minimizes steric effects, allowing a stronger, and thus shorter HB between interfacial methanol molecules. Such polar ordering at the interface might induce or nucleate the formation of chains, analogous to solid methanol, which would quickly branch into the less ordered hydrogen-bonded structure characteristic of the bulk liquid.

C. Methanol/water binary solutions

To further explore the surface sensitivity of TIY-detected XAS, we have begun a detailed study of the surface of methanol/water binary solutions. Methanol can be considered the simplest and weakest surfactant, showing positive absorption at the air/water interface of liquid water. SFG studies[4] of methanol/water suggest that methanol accumulates at the liquid interface, with evidence of polar ordering of the methyl group about surface normal.[63] Macroscopic measurements of surface tension also suggest that the methyl group is expelled from the interface, yielding ''hydrocarbon-like'' surface free energies for even dilute methanol/water solutions.[9]

Our XAS experiments consist of probing the surface of various bulk concentrations of methanol in water by interrogating the liquid microjet with 548 eV photons, which is well above the IP for both methanol and water. Ions produced by core-level excitation were extracted from the liquid surface and analyzed by a quadrupole mass spectrometer. Mass-resolved ion yields were then obtained as a function of bulk methanol mole fraction χ_{meth}. Carbon-containing fragments originating from methanol photoionization (e.g., C^+, CH^+, etc.) could be easily distinguished from water fragments (e.g., H_2O^+), allowing surface populations of both methanol and water to be obtained independently. In other words, XAS adsorption isotherms can be measured by collecting all mass fragments originating from either H_2O or CH_3OH photoionization as a function of χ_{meth}. In this way, the TIY measurement circumvents the need for individual cross sections for all of the different ion-fragmentation channels. This directly yields atomic oxygen populations at the liquid surface for both methanol and water in the binary solution. Shown in Fig. 14 are methanol and water TIY XAS adsorption isotherms normalized to the total ion signal of the pure liquids.

One can clearly see that the surface of the water/methanol solution is nonideal, thus exhibiting nearly monolayer coverage of methanol at a bulk mole fraction of ~0.1, indicating positive adsorption. This result illustrates the submonolayer surface sensitivity obtained in TIY XAS spectroscopy. The probe depth is estimated to be 2 Å, or 1 methanol molecular diameter, given the saturation of the mass-resolved TIY signal with increasing methanol mole fraction (χ_{meth}). In addition, there is some evidence for an inflection point ($\chi_{meth}\sim0.05$) in both the water and methanol isotherms, suggesting the importance of lateral interactions of clustering at the interface at submonolayer coverages of methanol.

To compare our results with macroscopic measurements of surface tension, we assume a simple model relating the surface tension of a binary solution to surface mole fraction. The surface tension of a binary solution (Γ_{CH_3OH/H_2O}) is assumed to be linear in *surface composition*[64]

$$\Gamma_{CH_3OH/H_2O}=\Gamma^0_{CH_3OH}X_{CH_3OH}+\Gamma^0_{H_2O}X_{H_2O}, \tag{8}$$

where Γ^0 is the surface tension of the pure liquids (H_2O and CH_3OH), and X_i is the surface mole fraction of either water or methanol determined by mass-resolved TIY XAS. Shown in Fig. 15 is the surface tension of the binary solution as a function of bulk χ_{meth} computed by Eq. (8). Also included for comparison are results of published surface tension mea-

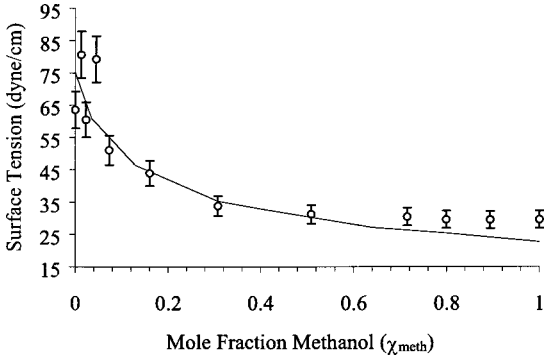

FIG. 15. Surface tension of the methanol/water binary solution determined by TIY XAS and Eq. (8). Solid line: previously published results from surface tension measurements of methanol/water solution at 20 °C (see Ref. 65).

surements for methanol/water solutions at 20 °C.[65] There is quantitative agreement between the macroscopic surface tension measurements and those determined here by the analysis of atomic O surface populations of methanol and water. There is slight deviation between the TIY XAS derived surface tension (at $\chi_{meth}=0.7$) and the previously published results. This deviation most probably indicates that the surface free energy is not only sensitive to the first liquid monolayer, but to subsequent layers beneath the surface that are not directly probed by TIY XAS. Similar conclusions have been drawn from SFG-derived surface excess measurements by Baldelli *et al.*[66]

The application of high-vacuum XAS techniques to liquid microjets allows a particular class of measurements to be performed on volatile liquid surfaces without significant interference from the equilibrium vapor. The temperatures of liquid jets injected into vacuum have been characterized. Larger jets (20 μm) remain near ambient temperature, and thus afford the possibility of examining the surface electronic structure of liquids under quasi-equilibrium conditions. Smaller diameter jets cool rapidly, creating the possibility for enhanced structural studies of low-temperature metastable liquids, which are difficult to address by other methods. The surface R_{O-O} distance has been characterized for both liquid methanol and water, indicating that significant differences in the surface hydrogen-bond topology exist between these apparently similar liquids. The direct determination of R_{O-O} represents a benchmark for MD simulations of liquid/vapor interfaces, hopefully assisting in the development of more refined liquid force fields. Monolayer sensitivity with a probe depth of $\sim$2 Å has been demonstrated using mass-resolved TIY XAS of methanol/water binary solutions. In addition, the direct determination of surface tension through TIY XAS directly links molecular-scale properties with macroscopic thermodynamic quantities, such as surface free energy.

ACKNOWLEDGMENTS

One of the authors (K. R. W.) is an Advanced Light Source Doctoral Fellow in Residence at Lawrence Berkeley National Laboratory. Three authors (D. T. C., R. D. S., and R. J. S.) are supported through the Experimental Physical Chemistry Program of the National Science Foundation. The authors thank Dr. John Bozek (ALS) for invaluable discussions throughout this continuing project. The authors also wish to acknowledge Dr. Jim Tobin (LLNL) for collaborations in the early phases of this work and B. Messer is also acknowledged for his assistance with the binary solution data. The XAS work was conducted at the Advanced Light Source, Lawrence Berkeley National Laboratory supported by the U.S. Department of Energy, under Contract No. DE-AC03-76SF00098.

[1] A. Braslau, M. Deutsch, P. S. Pershan, A. H. Weiss, J. Als-Nielsen, and J. Bohr, Phys. Rev. Lett. **54**, 114 (1985).
[2] E. Freysz, Q. Du, and Y. R. Shen, Ann. Phys. (Paris) **19**, 95 (1994).
[3] L. F. Scatena, M. G. Brown, and G. L. Richmond, Science **292**, 908 (2001).
[4] K. Wolfrum, H. Graener, and A. Laubereau, Chem. Phys. Lett. **213**, 41 (1993).
[5] D. E. Gragson, B. M. McCarty, and G. L. Richmond, J. Phys. Chem. **100**, 14272 (1996).
[6] M. E. King, G. M. Nathanson, M. A. Hanninglee, and T. K. Minton, Phys. Rev. Lett. **70**, 1026 (1993).
[7] K. L. Foster, R. A. Plastridge, J. W. Bottenheim, P. B. Shepson, B. J. Finlayson-Pitts, and C. W. Spicer, Science **291**, 471 (2001).
[8] P. Jungwirth and D. J. Tobias, J. Phys. Chem. B **105**, 10468 (2001).
[9] A. W. Adamson and A. P. Gast, *Physical Chemistry of Surfaces*, 6th ed. (Wiley, New York, 1997).
[10] M. Faubel, S. Schlemmer, and J. P. Toennies, Z. Phys. D: At., Mol. Clusters **10**, 269 (1988).
[11] M. Faubel and B. Steiner, Ber. Bunsenges. Phys. Chem. **96**, 1167 (1992).
[12] W. L. Holstein, L. J. Hayes, E. M. C. Robinson, G. S. Laurence, and M. A. Buntine, J. Phys. Chem. B **103**, 3035 (1999).
[13] G. D'Arrigo, G. Maisano, F. Mallamace, P. Migliardo, and F. Wanderlingh, J. Chem. Phys. **75**, 4264 (1981).
[14] D. E. Hare and C. M. Sorensen, J. Chem. Phys. **93**, 25–33 (1990).
[15] J. R. Scherer, M. K. Go, and S. Kint, J. Phys. Chem. **78**, 1304 (1974).
[16] G. E. Walrafen, M. S. Hokmabadi, and W. H. Yang, J. Chem. Phys. **85**, 6964 (1986).
[17] R. Vehring and G. Schweiger, Appl. Spectrosc. **46**, 25 (1992).
[18] K. L. Davis, K. Liu, M. Lanan, and M. D. Morris, Anal. Chem. **65**, 293 (1993).
[19] T. Muller, G. Grunefeld, and V. Beushausen, Appl. Phys. B: Lasers Opt. **70**, 155 (2000).
[20] H. Fuchs and H. Legge, Acta Astronaut. **6**, 1213 (1979).
[21] N. K. Adam, *The Physics and Chemistry of Surfaces*, 3rd ed. (Oxford University Press, London, 1941).
[22] G. Fang and C. A. Ward, Phys. Rev. E **59**, 417 (1999).
[23] C. A. Ward and D. Stanga, Phys. Rev. E **6405**, U347 (2001).
[24] C. A. Ward and G. Fang, Phys. Rev. E **59**, 429–440 (1999).
[25] D. Sibold and H. M. Urbassek, Phys. Fluids A **3**, 870 (1991).
[26] L. F. Phillips, Chem. Phys. Lett. **266**, 161 (1997).
[27] S. Myneni, Y. Luo, L. A. Naslund, M. Cavalleri, L. Ojamae, H. Ogasawara, A. Pelmenschikov, P. Wernet, P. Vaterlein, C. Heske, Z. Hussain, L. G. M. Pettersson, and A. Nilsson, J. Phys.: Condens. Matter **14**, L213 (2002).
[28] A. Filipponi, J. Phys.: Condens. Matter **13**, R23 (2001).
[29] A. Filipponi, J. Phys.: Condens. Matter **6**, 8415 (1994).
[30] J. Stöhr, *NEXAFS Spectroscopy* (Springer, Berlin, 1992).
[31] A. Bianconli, Appl. Surf. Sci. **6**, 392 (1980).
[32] R. Romberg, S. P. Frigo, A. Ogurtsov, P. Feulner, and D. Menzel, Surf. Sci. **451**, 116 (2000).
[33] F. Mafune, Y. Hashimoto, and T. Kondow, Chem. Phys. Lett. **274**, 127 (1997).
[34] T. Kondow and F. Mafune, Annu. Rev. Phys. Chem. **51**, 731 (2000).
[35] M. Faubel, B. Steiner, and J. P. Toennies, J. Electron Spectrosc. Relat. Phenom. **95**, 159 (1998).
[36] Q. Du, R. Superfine, E. Freysz, and Y. R. Shen, Phys. Rev. Lett. **70**, 2313 (1993).
[37] M. Matsumoto and Y. Kataoka, J. Chem. Phys. **88**, 3233 (1988).
[38] K. R. Wilson, M. Cavalleri, B. S. Rude, R. D. Schaller, A. Nilsson, L. G. M. Pettersson, N. Goldman, T. Catalano, J. D. Bozek, and R. J. Saykally, J. Phys.: Condens. Matter **14**, L221 (2002).

[39] D. T. Bowron, M. H. Krisch, A. C. Barnes, J. L. Finney, A. Kaprolat, and M. Lorenzen, Phys. Rev. B **62**, R9223 (2000).
[40] H. Bluhm, D. F. Ogletree, C. S. Fadley, Z. Hussain, and N. Salmeron, J. Phys.: Condens. Matter **14**, L227 (2002).
[41] D. Y. Kim, K. Lee, C. I. Ma, M. Mahalingam, D. M. Hanson, and S. L. Hulbert, J. Chem. Phys. **97**, 5915 (1992).
[42] L. G. M. Pettersson, A. Nilsson, S. Myneni, Y. Luo, M. Nyberg, M. Cavalleri, L. Ojamae, L. A. Naslund, H. Ogasawara, M. Odelius, and A. Pelmenschikov, J. Synchrotron Radiat. **8**, 136 (2001).
[43] D. Coulman, A. Puschmann, U. Hofer, H. P. Steinruck, W. Wurth, P. Feulner, and D. Menzel, J. Chem. Phys. **93**, 58 (1990).
[44] B. Rowland, M. Fisher, and J. P. Devlin, J. Chem. Phys. **95**, 1378 (1991).
[45] M. R. Watry, M. G. Brown, and G. L. Richmond, Appl. Spectrosc. **55**, 321A (2001).
[46] Y. R. Shen, Solid State Commun. **84**, 171 (1992).
[47] M. E. Saecker, S. T. Govoni, D. V. Kowalski, M. E. King, and G. M. Nathanson, Science **252**, 1421 (1991).
[48] I. Benjamin, M. A. Wilson, A. Pohorille, and G. M. Nathanson, Chem. Phys. Lett. **243**, 222 (1995).
[49] D. C. Koningsberger and R. Prins, *X-ray Absorption: Principles, Applications, Techniques of EXAFS, SEXAFS, and XANES* (Wiley, New York, 1988).
[50] B. K. Teo, *EXAFS: Basic Principles and Data Analysis* (Springer, Berlin, 1986).
[51] K. R. Wilson, R. D. Schaller, D. T. Co, R. J. Saykally, B. S. Rude, T. Catalano, and J. D. Bozek, J. Chem. Phys. **117**, 7738 (2002).
[52] K. V. Klementev, Nucl. Instrum. Methods Phys. Res. A **448**, 299 (2000).
[53] A. K. Soper, Chem. Phys. **258**, 121 (2000).
[54] G. Hura, J. M. Sorenson, R. M. Glaeser, and T. Head-Gordon, J. Chem. Phys. **113**, 9140 (2000).
[55] L. X. Dang and T. M. Chang, J. Chem. Phys. **106**, 8149 (1997).
[56] R. M. Townsend and S. A. Rice, J. Chem. Phys. **94**, 2207 (1991).
[57] R. S. Taylor, L. X. Dang, and B. C. Garrett, J. Phys. Chem. **100**, 11720 (1996).
[58] A. K. Adya, L. Bianchi, and C. J. Wormald, J. Chem. Phys. **112**, 4231 (2000).
[59] T. Weitkamp, J. Neuefeind, H. E. Fischer, and M. D. Zeidler, Mol. Phys. **98**, 125 (2000).
[60] C. D. Stanners, Q. Du, R. P. Chin, P. Cremer, G. A. Somorjai, and Y. R. Shen, Chem. Phys. Lett. **232**, 407 (1995).
[61] K. J. Tauer and W. N. Lipscomb, Acta Crystallogr. **5**, 606 (1952).
[62] S. Sarkar and R. N. Joarder, J. Chem. Phys. **99**, 2032 (1993).
[63] M. Matsumoto and Y. Kataoka, J. Chem. Phys. **90**, 2398 (1989).
[64] J. G. Eberhart, J. Phys. Chem. **70**, 1183 (1966).
[65] *CRC Handbook of Chemistry and Physics*, 62nd ed., edited by D. R. Lide (CRC Press, Boca Raton, FL, 1981).
[66] S. Baldelli, C. Schnitzer, M. J. Shultz, and D. J. Campbell, J. Phys. Chem. B **101**, 4607 (1997).